Evidence of Polaron Formation in Halide Perovskites via Carrier Effective Mass Measurements

Di Bao,[1,‡] Qing Chang,[1,‡] Bingbing Chen,[2] Xiaoxuan Chen,[1] Handong Sun,[1] Yeng Ming Lam,[2] Daming Zhao,[1] Jian-Xin Zhu,[3,†] and Elbert E.M. Chia[1,*]

[1] *Division of Physics and Applied Physics, School of Physical and Mathematical Sciences, Nanyang Technological University 637371, Singapore*

[2] *School of Materials Science and Engineering, Nanyang Technological University 639798, Singapore*

[3] *Theoretical Division and Center for Integrated Nanotechnologies, Los Alamos National Laboratory, Los Alamos, New Mexico 87545, United States*

(Received 8 May 2022; revised 6 January 2023; accepted 9 January 2023; published 2 February 2023; corrected 16 February 2023)

Carrier effective mass is a central parameter in solid-state physics. It is a measure of the strength of the coupling between a carrier and excitations arising from its surrounding medium, and features prominently in transport and optical calculations. Experimental techniques employed to determine it are steady-state ones, and so are unable to detect any change in the effective mass after a strong perturbation to the system, e.g., strong optical excitation. By combining time-resolved terahertz spectroscopy and transient absorption spectroscopy, on a mixed-cation mixed-halide perovskite thin film, we observe a large and long-lived photoinduced enhancement of the carrier effective mass, and from it deduce a twofold increase of the carrier-phonon coupling constant, giving evidence of polaron formation. Our work demonstrates a new approach to track the strength and ultrafast lifetimes of photoinduced carrier-boson interactions down to picosecond timescales that can be applied to a wide range of solid-state systems.

DOI: 10.1103/PRXEnergy.2.013001

I. INTRODUCTION

In solid-state systems, the electrons (or carriers) are always "dressed," i.e., they couple to collective modes called bosons that arise from their surroundings, for example, phonons arising from lattice distortions [1]. The quasiparticle that results from such electron-boson coupling will have an effective mass m^* that is different from the bare electron mass m_0, where the deviation of m^* from m_0 is a measure of the strength of the electron-boson coupling. Experimentally, m^* is measured using techniques such as cyclotron resonance [2], angle-resolved photoemission [3], and the optical Hall effect [4], but these are steady-state techniques. The time-resolved change in m^* has been reported using time-resolved magnetoterahertz spectroscopy on semiconductor InSb [5]. In solar cell materials, m^* enters directly into the calculation of carrier density and mobility, which enables the calculation of the carrier diffusion length and carrier recombination kinetics [6,7], both of which are crucial solar cell device parameters. However, the value of m^* used in these calculations is always that obtained from steady-state techniques, which assumes that the effective mass does not change after photoillumination.

As a result of the many-body interaction in halide perovskites, polarons arise from the coupling between the carriers and the distorted lattice, and has been studied using experimental spectroscopic methods. Previous studies have revealed the existence of polaron formation in halide perovskites using femtosecond optical Kerr effect spectroscopy [8], optical pump-terahertz probe spectroscopy [9,10], and far-infrared photoinduced absorption spectroscopy [11]. Although the above methods have provided indirect evidence for polaron formation, such as the long decay in the optical Kerr signal [8], deviation from a Drude model of the terahertz response [9], and spectral changes in photoinduced absorption [11], a more direct way would be to experimentally track the time evolution of m^*, together with the associated electron-phonon coupling α. Recently, a time-resolved x-ray scattering and transient reflection study extracted m^* in the halide perovskite $CH_3NH_3PbI_3$, and showed that there is indeed a change after photoexcitation, with m^* reaching a maximum

*elbertchia@ntu.edu.sg
†jxzhu@lanl.gov
‡These authors contributed equally to this work.

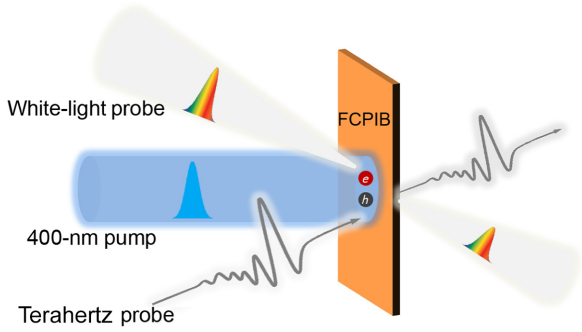

FIG. 1. A schematic of our TA and frequency-resolved TRTS experiments. A 400-nm pulse laser is used to pump the FCPIB sample, followed by a white-light probe and terahertz probe to investigate the carrier dynamics in the sample.

at 20 ps [12]. However, that work was only able to obtain a normalized effective mass relative to its maximum value, not the absolute value of m^*, and they attributed its enhancement to the change of the electronic band curvature. In our work, we employ (a) frequency-resolved and time-resolved terahertz spectroscopy (TRTS) and (b) transient absorption (TA) (see Fig. 1) in the mixed-cation mixed-halide perovskite $FA_{0.85}Cs_{0.15}Pb(I_{0.97}Br_{0.03})_3$ (FCPIB) to estimate the value of m^* and its time evolution after photoexcitation. We find that, immediately after photoexcitation, m^* starts increasing from about $0.2m_0$ at 0.5 ps, which is close to the values predicted by theoretical calculations [13–17] and experimental measurements [18] for the halide perovskites. It monotonically increases, reaches a maximum value at about 200 ps, and thereafter decreases gradually. Even at 3 ns, m^* is still significantly larger than its preexcitation value. The carrier cooling via a carrier-phonon interaction model, which is backed up by a microscopic model analysis, reveals a twofold increase in the carrier-phonon coupling constant upon photoexcitation. This, together with the large and persistent enhancement of m^*, is evidence of the presence of strong polaronic effects in the halide perovskites [9,19–21]. Our work demonstrates the use of the combination of TRTS and TA to obtain the photoinduced enhancement of m^* and its time evolution, which not only sheds light on the strength and lifetime of the carrier-phonon interaction in this class of solar cell materials, but can also be applied to many other classes of solid-state systems.

II. RESULTS AND DISCUSSION

A. Time-resolved terahertz spectroscopy

We perform frequency-resolved TRTS to investigate the photogenerated carriers in the FCPIB thin film (see Appendix A). By measuring the transmitted terahertz electric waveform of the sample (FCPIB/z-cut quartz) and reference (z-cut quartz) without optical excitation [see Fig. 2(a)], we extract the complex optical conductivity $\tilde{\sigma}(\omega) = \sigma_1(\omega) + i\sigma_2(\omega)$ at room temperature, as the orange line shows in Fig. 2(b). Two peaks at about 0.9 THz and about 1.7 THz are observed, which correspond to two transverse-optical phonon absorption features [10]. Then the FCPIB sample is excited with a 60-fs, 400-nm pump pulse to perform frequency-resolved TRTS by varying the optical path (thus time delay) between the 400-nm pump pulse and the terahertz pulse (see Appendix B 1 for experimental details), from which we obtain the photoconductivity $\Delta\sigma(\omega)$ for different time delays [10], as shown in Figs. 2(c) and 2(d). The frequency-resolved photoconductivity not only shows the Drude-like response from the photogenerated free charge carriers, but also a derivativelike profile located near the two phonon features as shown in Figs. 2(c) and 2(d). Such features are attributed to the existence of carrier-phonon coupling [10]. To model the photoconductivity, we employ a combination of Drude-Smith and peak-shift contributions to extract information about the photoexcited carriers, given by $\Delta\tilde{\sigma}(\omega) = \Delta\tilde{\sigma}_{\mathrm{DS}} + \Delta\tilde{\sigma}_{\mathrm{PS}}$. The Drude-Smith term is given by

$$\Delta\tilde{\sigma}_{\mathrm{DS}} = \left(\frac{\omega_{pD}^2\epsilon_0}{\gamma}\right)\frac{1}{1-i2\pi f/\gamma}\left(1+\frac{c_1}{1-i2\pi f/\gamma}\right), \tag{1}$$

where ω_{pD} is the plasma frequency, ϵ_0 is the vacuum permittivity, γ is the carrier scattering rate, and c_1 defines the fraction of the carrier's initial velocity that is retained after experiencing a collision. The peak-shift term is introduced to account for a change in the phonon profile in the presence of free carriers [10], given by

$$\Delta\tilde{\sigma}_{\mathrm{PS}} = \sum_{k=1,2}\left\{\frac{\epsilon_0\omega}{i(\omega_k^2-\omega)+\omega\gamma_k}\Delta\omega_{pk}^2 + \frac{-2i\omega_k\epsilon_0\omega_{p,k}^2\omega}{[i(\omega_k^2-\omega^2)+\omega\gamma_k]^2\Delta\omega_k}\right\} - i\epsilon_0\omega\Delta\epsilon_\infty, \tag{2}$$

where ω_k is the phonon resonance frequency, γ_k is the damping rate of the kth phonon mode, ϵ_∞ is the background dielectric constant, $\Delta\omega_{p,k}^2$ is the phonon spectral weight change, $\Delta\omega_k$ is the phonon frequency shift, and $\Delta\epsilon_\infty$ is the change in the background dielectric constant. In our case, the summation is over the two phonon modes resolved in Fig. 2(b). Parameters such as ω_k, γ_k, and ϵ_∞ are obtained from a Lorentzian fit to the phonon modes of the terahertz spectrum at equilibrium (see the Supplemental Material [22]), while $\Delta\omega_{p,k}^2$, $\Delta\omega_k$, $\Delta\epsilon_\infty$, ω_{pD}, and γ are obtained using the "Drude-Smith + peak-shift model" to fit the photoconductivity at different time delays. Then we extract the Drude plasma frequency ω_{pD} and scattering rate γ. Most TRTS studies typically assume a time-independent carrier mobility $\mu(\tau)$ and carrier effective mass $m^*(\tau)$, so that the carrier density N can be

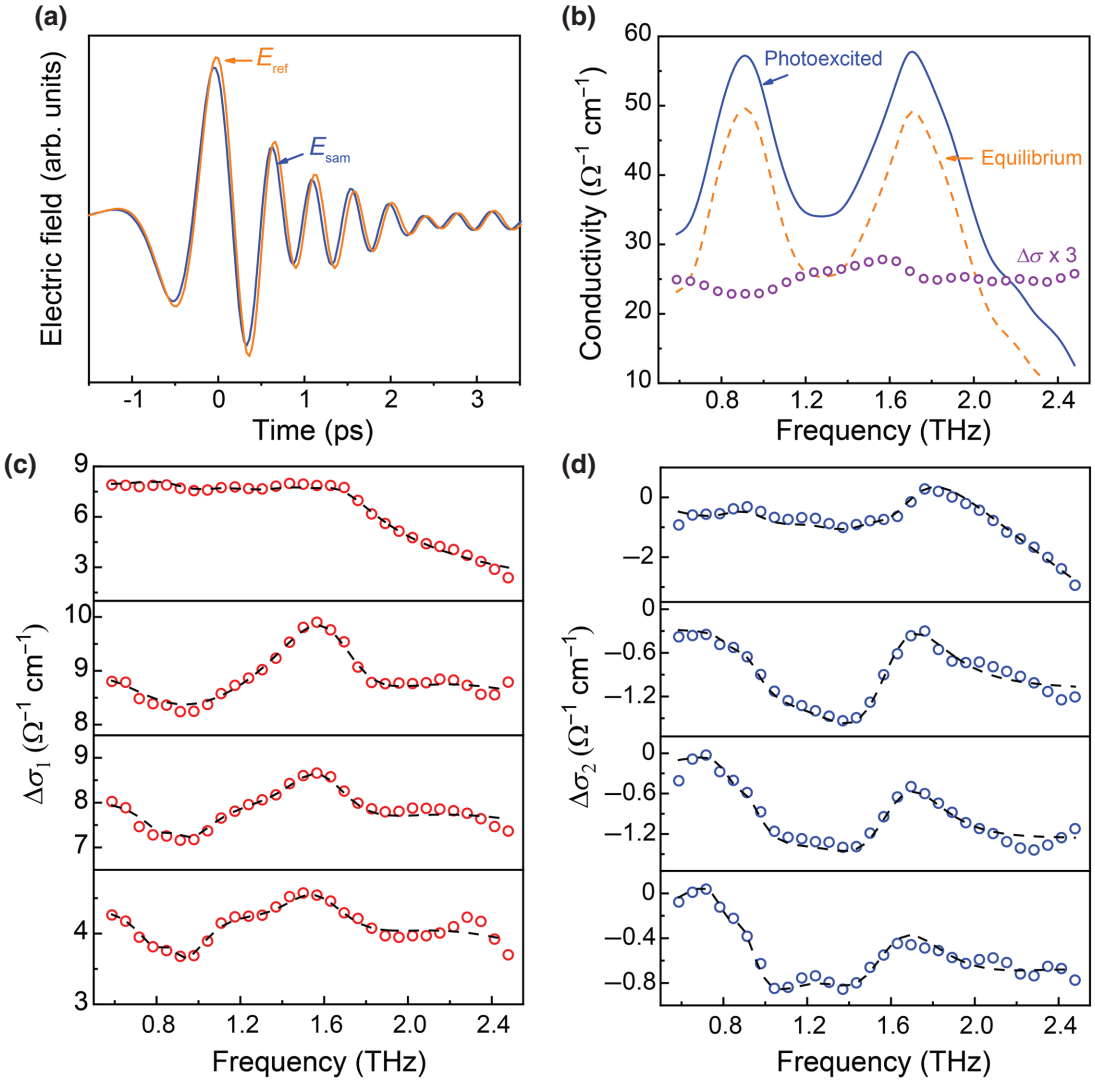

FIG. 2. Frequency-resolved, time-resolved THz spectroscopy. (a) THz time-domain waveform passing through the sample (FCPIB film/z-cut quartz, orange line) and reference (z-cut quartz, blue line). (b) Real part of the photoconductivity (purple) obtained as the difference between the photoexcited (blue) and equilibrium (orange) THz conductivities. The peaks originate from two transverse-optical phonon absorption features. (c) Real and (d) imaginary parts of the THz photoconductivity at different time delays [1, 10, 100, 1000 ps (in order from top to bottom)]. The dashed lines are the fits by the "Drude-Smith + peak-shift model".

calculated by

$$\omega_p^2 = \frac{Ne^2}{\epsilon_0 m^*}. \tag{3}$$

This equation therefore does not take into account any possible photoinduced change of $m^*(\tau)$. In our analysis, we leave m^* as an unknown quantity. Later we show that there is indeed a large photoenhancement of m^*, and that m^* is a strong function of time delay after photoexcitation.

B. Steady-state and transient absorption spectra

We next measure the steady-state and transient absorption spectra of the FCPIB sample (see Appendix B). Figure 3 shows the steady-state absorption spectrum with an absorption edge at about 1.6 eV and thereafter a monotonic increase of absorbance with increasing photon energy. By employing Elliott's formula with a non-parabolic band [24–28], given by

$$A(\hbar\omega) = A_C(\hbar\omega) + A_E(\hbar\omega), \tag{4}$$

where the carrier contribution term is

$$A_C(\hbar\omega) = A_1 \frac{2\pi\sqrt{E_b}}{\hbar\omega} \frac{1}{\Gamma} \int_{E_g}^{\infty} \operatorname{sech}\left(\frac{\hbar\omega - E}{\Gamma}\right) \frac{\xi(E - E_g)}{1 - \exp(-2\pi\sqrt{E_b/(E - E_g)})} dE \tag{5}$$

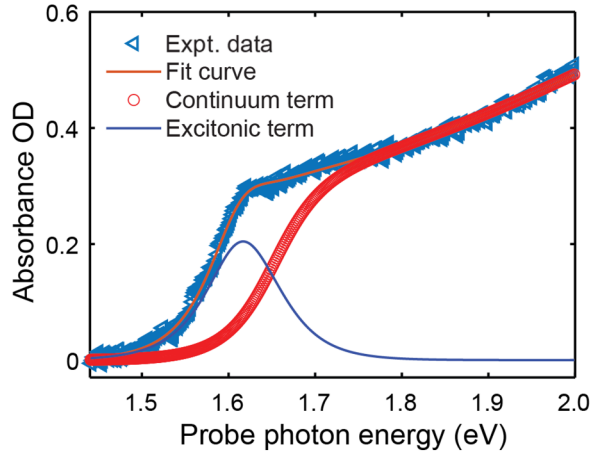

FIG. 3. Steady-state absorption spectrum. The continuum term and excitonic term are disentangled from the fits by Eq. (4). OD is the optical density defined by $\log_{10}(I_1/I_0)$, where I_0 is the incident intensity and I_1 is the transmitted intensity.

and the exciton contribution (EC) term is

$$A_E(\hbar\omega) = A_2 \frac{2\pi {E_b}^{3/2}}{\hbar\omega} \frac{1}{\Gamma} \sum_{j=1}^{j_{\max}=7} \frac{1}{j^3} \operatorname{sech}\left(\frac{\hbar\omega - E_g + E_b/j^2}{\Gamma}\right), \tag{6}$$

with prefactors A_1 and A_2 proportional to the transition dipole moment, E_g is the band gap, E_b is the exciton binding energy, $E_g - E_b/j^2$ is the energy of the j^{th} excitonic state with $j_{\max}$ the cutoff (we choose $j_{\max} = 7$, which is high enough to account for all excitonic contributions to the absorption spectrum), the $E_b^{3/2}$ in the EC term arises from the coupling between the wave functions of an electron and a hole [29], Γ is the exciton bandwidth, and $\xi(E - E_g) = 1 + 10R(E - E_g) + 126R^2(E - E_g)^2$ accounts for the band nonparabolicity effect with R the nonparabolic factor [27]. With the fitting curve as shown in Fig. 1(b), we resolve the continuum contribution (red circles) with $E_g = 1.653 \pm 0.005$ eV and the exciton contribution (blue curve) with $E_b = 38 \pm 4$ meV. The fitted values of E_g and E_b are consistent with reported values in FA-based halide perovskites [10,30–33].

With the information obtained from the steady-state absorption spectrum, we next measure the TA spectra of FCPIB with 400-nm pump pulse excitation. Figure 4(a) shows the normalized TA spectra at representative time delays ranging from 0.7 ps to 2.6 ns with a pump fluence of 18 μJ/cm^2. A typical photoinduced bleaching feature (positive part) is observed, indicating the filling of the excited states by photoexcited carriers and excitons. The quick thermalization among the hot carriers yields a population distribution that obeys the Fermi-Dirac (FD) distribution. When the energy of interest is much larger than the Fermi energy, the FD distribution can be simplified to the Maxwell-Boltzmann (MB) distribution [6,34], given by

$$-\Delta A(\hbar\omega) \propto \exp\left(-\frac{\hbar\omega}{k_B T_e}\right), \tag{7}$$

where k_B is the Boltzmann constant and T_e is the carrier temperature. By using Eq. (7) to fit the high-energy tail of the TA spectra in Fig. 4(a), we extract the time evolution of T_e as shown in Fig. 4(b) for three pump fluences. For all pump fluences, T_e shows a slow cooling trend due to the presence of a hot phonon bottleneck.

With the input of carrier temperature T_e and the parameters from the steady-state absorption spectrum, we then use the Elliot model to fit the TA spectra by considering the photoinduced change in both the carrier term [Eq. (5)] and exciton term [Eq. (6)]. The photoinduced change in the carrier term is given by

$$\begin{aligned}
\Delta A_C(\hbar\omega) &= A_C'(E_b', E_g', \hbar\omega)(1 - f_{\text{FD}})^2 - A_C(\hbar\omega), \\
&= f_1 A_1 \frac{2\pi\sqrt{E_b'}}{\hbar\omega} \frac{1}{\Gamma'} \int_{E_g'}^{\infty} \operatorname{sech}\left(\frac{\hbar\omega - E}{\Gamma'}\right) \\
&\quad \times \frac{\xi(\hbar\omega - E_g')}{1 - \exp(-2\pi\sqrt{E_b'/(E - E_g')})} dE \\
&\quad \times \left(1 - \frac{1}{1 + \exp((\hbar\omega - E_f)/k_B T_e)}\right)^2 \\
&\quad - A_1 \frac{2\pi\sqrt{E_b}}{\hbar\omega} \frac{1}{\Gamma} \int_{E_g}^{\infty} \operatorname{sech}\left(\frac{\hbar\omega - E}{\Gamma}\right) \\
&\quad \times \frac{\xi(\hbar\omega - E_g)}{1 - \exp(-2\pi\sqrt{E_b/(E - E_g)})} dE,
\end{aligned} \tag{8}$$

where E_b' and E_g' are the exciton binding energy and band gap, respectively, after photoexcitation, prefactor f_1 accounts for the photoinduced change in the transition dipole moment in A_1 (f_1 is found to be about 1 in the fittings and so will be fixed as 1 in our fits), and the $(1 - f_{\text{FD}})^2$ term represents the state-filling effect in the conduction band (electrons) and valence band (holes) with f_{FD} the Fermi-Dirac distribution function characterized by the carrier temperature T_e and the quasi-Fermi energy E_f. Here we assume a negligible change in the nonparabolic coefficient R, nearly equal electron and hole effective masses, and carrier temperatures $T_e \approx T_h$ (T_h is the temperature of

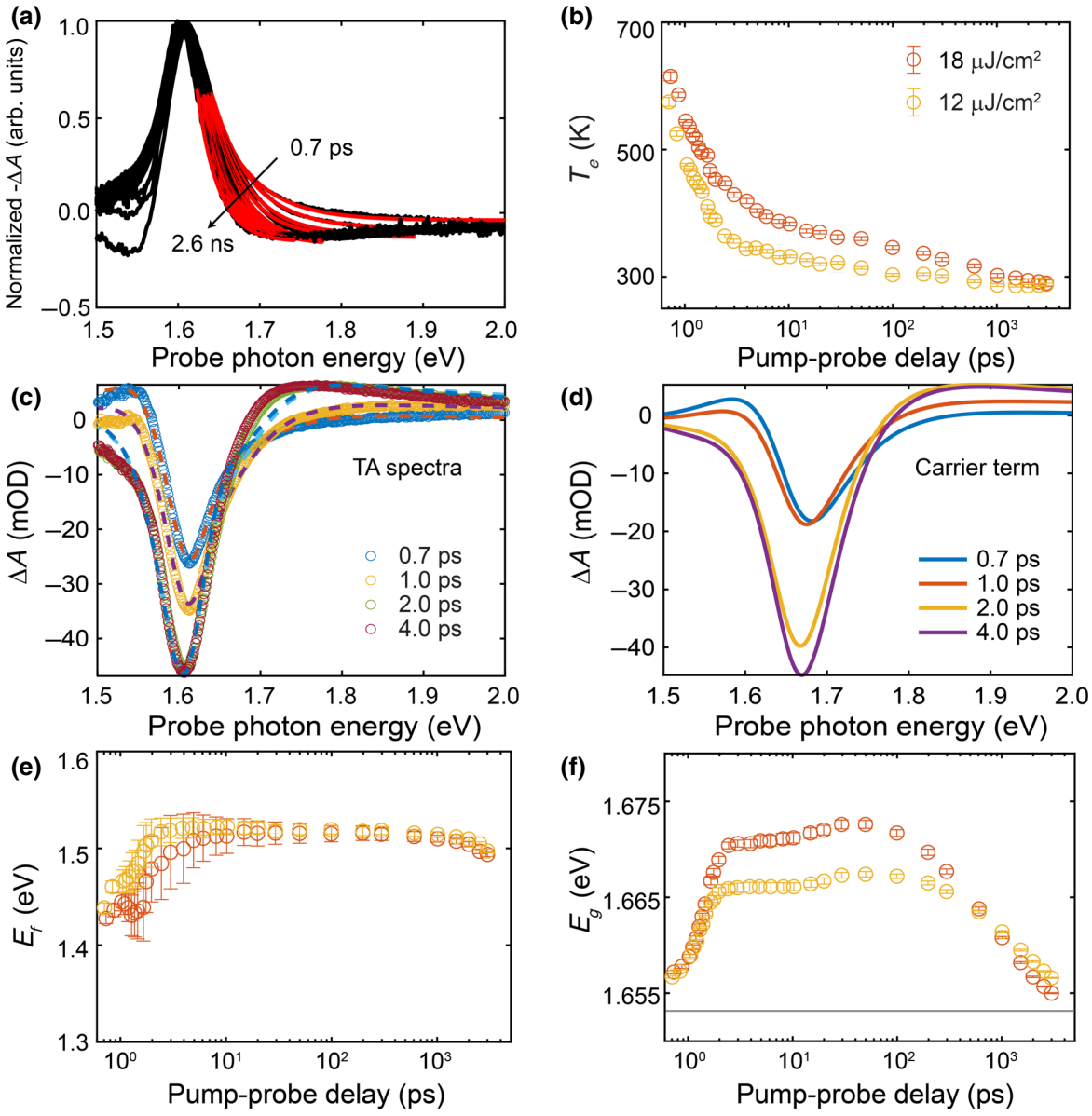

FIG. 4. (a) Normalized TA spectra with a pump fluence of 18 μJ/cm^2 under a 400-nm pump ranging from 0.7 ps to 2.6 ns. The red lines are the MB fit curves. (b) Carrier temperatures extracted from the MB fits as a function of pump-probe delay. (c) Transient absorption spectra for experimental data (circles) and fits (dashed lines) at representative time delays. The carrier contribution terms at representative time delays are shown in (d). In (c) and (d), mOD is milli-OD, where OD has been defined in the caption of Fig. 3. (e),(f) Extracted Fermi energy E_f and band gap E_g as a function of pump-probe delay.

holes). The exciton term is expressed as

$$\begin{aligned}\Delta A_E(\hbar\omega) &= f_2 A'_E(E'_b, E'_g, \Gamma', \hbar\omega) - A_E(\hbar\omega),\\ &= f_2 A_2 \frac{2\pi\sqrt{E'_b}}{\hbar\omega}\frac{1}{\Gamma'}\sum_{j=1}^{7}\frac{2E'_b}{j^3}\,\mathrm{sech}\left(\frac{\hbar\omega - E'_g + E'_b/j^2}{\Gamma'}\right)\\ &\quad - A_2\frac{2\pi\sqrt{E_b}}{\hbar\omega}\frac{1}{\Gamma}\sum_{j=1}^{7}\frac{2E_b}{j^3}\,\mathrm{sech}\left(\frac{\hbar\omega - E_g + E_b/j^2}{\Gamma}\right),\end{aligned} \tag{9}$$

where prefactor f_2 implies the photoinduced change in the exciton oscillator strength [29].

With Eqs. (8) and (9), the TA spectra $\Delta A(\hbar\omega)$ can be fit via

$$\Delta A(\hbar\omega) = \Delta A_C(\hbar\omega) + \Delta A_E(\hbar\omega), \tag{10}$$

using T_e from the MB fits to the TA spectra, while A_1, A_2, E_b, E_g, and Γ are obtained from the fit of the steady-state absorption spectrum earlier, as given in Eqs. (5) and (6).

We then obtain the fitting parameters E_b', E_g', Γ', f_2, and E_f. Figure 4(c) shows the fitting curves to the ΔA spectra, while the corresponding carrier terms are plotted in Fig. 4(d). The bleaching dip in Fig. 4(c) arises from the state filling of both hot carriers and exciton states. As the pump-probe time delay increases from 0.7 to 4.0 ps, the bleaching dip of the carrier terms shows a red shift, suggesting that the carriers lose energy (via carrier-phonon coupling) and cool down to the band edge. The amplitude of the bleaching dip also increases since a large number of carriers gradually accumulate near the band edge that strongly quenches the band-edge absorption.

From the fitting, we are able to extract the time evolution of important parameters: Fermi energy E_f and band gap E_g, as shown in Figs. 4(e) and 4(f). The Fermi energy E_f shows an increase from the onset after photoexcitation, suggesting that more carriers are promoted into the conduction band. At longer time delays (after about 1 ns), the E_f starts to decrease but very slowly, suggesting a long lifetime for the photoexcited carriers. At the same time, the band gap E_g shows a positive change relative to the original band gap [the black line in Fig. 4(f)]. For conventional inorganic semiconductors such as the heavily Sn-doped In_2O_3, the optical band gap is reported to increase with carrier density [35]. The change in the band gap is attributed to two mechanisms: (1) the Burstein-Moss effect and (2) band-gap renormalization (BGR) [35–37]. The former effect promotes the interband transition to higher energies due to the filling of the states near the band edge by the carriers, thus enlarging the band gap [36,38]. The latter BGR term typically reduces the band gap as a result of mutual exchange and Coulomb interactions between the excited free electrons in the conduction band, as well as electron impurity scattering [37,38]. However, it is reported that lead halide perovskites exhibit an atypical temperature-induced band-gap renormalization, that is, the band gap *increases* with increasing temperature, due to the thermal expansion and electron-phonon interactions [30,39,40], as compared to the typical band-gap decrease in inorganic semiconductors [41]. Therefore, the atypical increase in the band gap in Fig. 4(f) is not inconsistent with temperature-dependent band-gap measurements.

C. Carrier effective mass evolution and polaron dynamics

From the parameters E_g, E_f, and T_e obtained from analysis of TA data, we can calculate the electron density N_e via the expression $N_e = \int_{E_g}^{\infty} D_c(\hbar\omega) f_{\mathrm{FD}} d\hbar\omega$, where $D_c(\hbar\omega)$ is the density of states in the conduction band [6]. The full formula is given by

$$N_e = \int_{E_g}^{\infty} \frac{1}{2\pi^2}\left(\frac{2m^*}{\hbar^2}\right)^{3/2}\sqrt{E-E_g} \times \frac{\xi(E-E_g)}{1+\exp((E-E_f)/k_BT)}dE. \tag{11}$$

Since the carrier densities in the TRTS and TA measurements are the same, we can combine Eq. (3) from TRTS and Eq. (11) from TA to extract the electron effective mass m^* as a function of pump-probe delay τ by the expression

$$m^*(\tau) = \left[\frac{\omega_p^2\epsilon_0}{e^2\int_{E_g}^{\infty}(1/2\pi^2)(2/\hbar^2)^{3/2}\sqrt{E-E_g}\{\xi(E-E_g)/[1+\exp((E-E_f)/k_BT)]\}dE}\right]^2. \tag{12}$$

Here we calculate m^* with Eq. (12), scaled by the free electron mass m_0, as shown in Fig. 5(a). At about 0.5 ps, we obtain $m^* \sim 0.2m_0$ for fluences of 18 and 12 μJ/cm^2, which is close to the steady-state effective mass of about $0.24m_0$ for the halide perovskites [6,13–18,42], giving credence to our approach. The value of m^* increases rapidly after 1 ps, suggesting a strong dressing of the electron by its surrounding environment. Figure 5(a) shows that m^* quickly increases after photoexcitation and reaches a maximum at about 200 ps. The increase in m^* can be associated with the polaron formation that is associated with short-range lattice distortion [12]. When such localized strong fields expand to larger length scales due to carrier delocalization, we expect a decrease of m^*, which is observed about 200 ps after photoexcitation. It is interesting to see that m^*/m_0 does not recover to its preexcitation value even at 2.6 ns, suggesting a long lifetime of the polarons.

We repeat the data fitting and analysis using the "Drude + peak-shift model", that is, without the Smith term. Compared to the "Drude-Smith + peak-shift model", the fit quality is worse at high frequencies (see Fig. S4 within the Supplemental Material [22]), and the obtained values of m^* differed by at most 50% at 250 ps [see Fig. 5(b)]. Hence, the obtained value of m^* sensitively depends on the model used, and is only an estimate. However, the overall trend remains robust against the model used, that is, m^* peaks at about 200 ps. Using the same method, we also obtained m^* for $CH_3NH_3PbI_3$, finding that m^* peaks at about 20 ps (instead of 200 ps in FCPIB) (see the Supplemental Material [22] for the analysis of $CH_3NH_3PbI_3$).

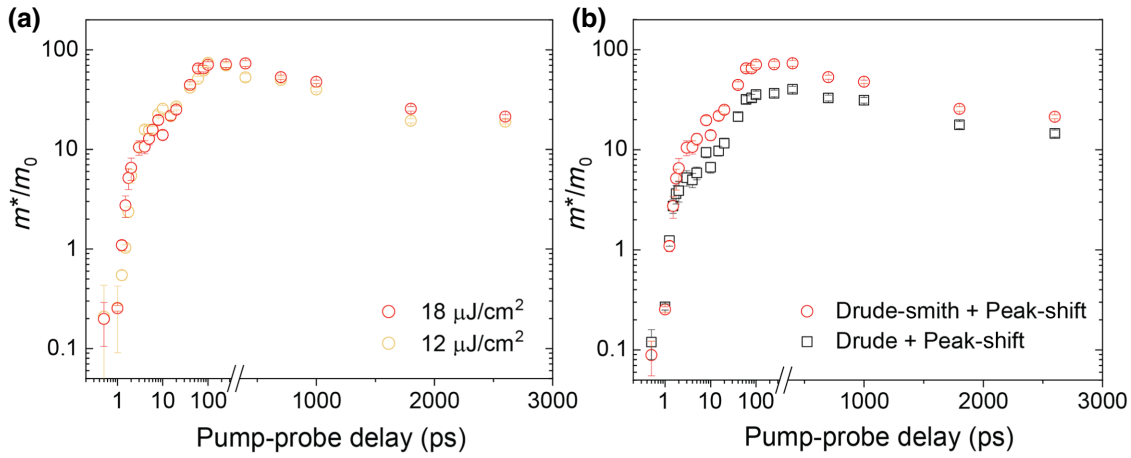

FIG. 5. Ultrafast transient change of polaron formation and relaxation. (a) Calculated effective mass of electrons using the "Drude-Smith + peak-shift model". (b) Comparison of m^* obtained by using the "Drude-Smith + peak-shift model", and "Drude + peak-shift model".

The change in m^* arises from many-body interactions, which can in general be the electron-phonon and electron-electron interactions. The electron-electron interaction is negligible in the perovskites, and the electron-phonon interaction is strong and leads to the formation of polarons [9,19–21]. From polaron theory, in the large polaron limit, the effective mass is given by $m^* = m_b(1 + \alpha/6 + 0.0236\alpha^2)$, where m_b is the band mass (i.e., electron mass derived from band curvature) and α is the electron-phonon coupling constant. Therefore, a photoinduced increase in m^* can originate from an increase in m_b, or α, or both. In order to obtain α, we fit the T_e versus τ data to a model where the photoexcited electrons lose energy to the LO phonon mode, given by [6]

$$\frac{dU_c}{d\tau} = \frac{3k_B}{2}\frac{dT_e}{d\tau} \approx \frac{-\hbar\omega_{\mathrm{LO}}}{\tau_{\mathrm{ave}}}\left[\exp\left(-\frac{\hbar\omega_{\mathrm{LO}}}{k_B T_e}\right) - \exp\left(-\frac{\hbar\omega_{\mathrm{LO}}}{k_B T_{\mathrm{ph}}}\right)\right], \tag{13}$$

where T_{ph} is the lattice temperature and $\hbar\omega_{\mathrm{LO}}$ is the LO phonon energy. The data and fitting curves are shown in Fig. 6 for the first 20 ps. For the fluence of 18 μJ/cm^2, $\tau_{\mathrm{ave}} = 77 \pm 6$ fs. From this value of τ_{ave}, and the effective LO phonon energy $\omega_{\mathrm{LO}}/2\pi = 3.45$ THz, we can obtain α from the expression $\alpha = \tau_{\mathrm{ave}}^{-1}/(\omega_{\mathrm{LO}}/2\pi)$ (see Appendix C for the derivation) to be 3.8. This value of α is about 2 times the steady-state (or preexcitation) value of about 1.7 [10], showing that there is indeed an enhancement in the electron-phonon coupling upon photoexcitation, consistent with the picture that polarons are indeed formed in the perovskites after photoillumination.

An increase of α from the steady-state value of 1.7 to a photoenhanced value of 3.8 results in an increase of the $(1 + \alpha/6 + 0.0236\alpha^2)$ factor from 1.4 to 2—about a 50% increase. This alone cannot account for the increase in m^*/m_0 values that we see in Fig. 5(a), strongly suggesting that the band mass m_b must also increase upon photoillumination. A recent time-resolved x-ray scattering and transient reflection paper [12], which observed an increase in the (normalized) m^* upon photoexcitation, attributed the increase to the change in band curvature when electronic states near the conduction band minimum are filled, thereby changing the effective mass m^*.

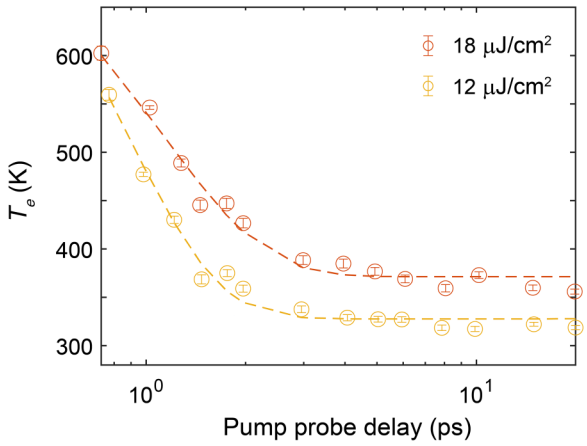

FIG. 6. Carrier temperature cooling curves within the first 20 ps.

We next present a microscopic model that explains the photoenhancement of m^*. We consider the effect of coupling between electrons and hot phonons. Within a two-temperature model, as described by the electronic temperature T_e and phonon temperature $T_{\rm ph}$, the electronic self-energy arising from the electron-phonon interaction is given by [43]

$$\Sigma(\mathbf{k},\omega) = \frac{g^2}{N_L}\sum_{\mathbf{q}}\left[\frac{n_B(\omega_{\mathbf{q}},T_{\rm ph}) + n_{\rm FD}(-\xi_{\mathbf{k}-\mathbf{q}},T_e)}{\omega - \xi_{\mathbf{k}-\mathbf{q}} - \hbar\omega_{\mathbf{q}} + i\eta} + \frac{n_B(\omega_{\mathbf{q}},T_{\rm ph}) + n_{\rm FD}(\xi_{\mathbf{k}-\mathbf{q}},T_e)}{\omega - \xi_{\mathbf{k}-\mathbf{q}} + \hbar\omega_{\mathbf{q}} + i\eta}\right]. \tag{14}$$

Here we have neglected the momentum dependence of the electron-phonon coupling matrix and represented the coupling strength by g, N_L is the number of lattice sites, and quantities $\hbar\omega_{\mathbf{q}}$ and $\xi_{\mathbf{k}}$ are the phonon and electron energy dispersions, respectively. For the latter, the energy is measured with respect to an effective Fermi energy, and η is a positive infinitesimal. The Bose-Einstein distribution function is

$$n_B(\omega) = \frac{1}{\exp(\hbar\omega/k_B T_{\rm ph}) - 1}, \tag{15}$$

while the Fermi-Dirac distribution function is

$$n_{\rm FD}(\xi) = \frac{1}{\exp(\xi/k_B T_e) + 1}. \tag{16}$$

We focus on the longitudinal optical phonon mode and consider an Einstein approximation $\omega_{\mathbf{q}} = \omega_{\rm LO}$. The momentum-averaged self-energy is given by

$$\begin{aligned}\Sigma(\omega) &= \frac{1}{N_L}\sum_{\mathbf{k}}\Sigma(\mathbf{k},\omega)\\ &= g^2\int d\xi\rho(\xi)\left[\frac{n_B(\omega_{\rm LO},T_{\rm LO}) + n_{\rm FD}(-\xi,T_e)}{\omega - \xi - \hbar\omega_{\rm LO} + i\eta} + \frac{n_B(\omega_{\rm LO},T_{\rm LO}) + n_{\rm FD}(\xi,T_e)}{\omega - \xi + \hbar\omega_{\rm LO} + i\eta}\right]\\ &= g^2\rho(0)\int d\xi\left[\frac{n_B(\omega_{\rm LO},T_{\rm LO}) + n_{\rm FD}(-\xi,T_e)}{\omega - \xi - \hbar\omega_{\rm LO} + i\eta} + \frac{n_B(\omega_{\rm LO},T_{\rm LO}) + n_{\rm FD}(\xi,T_e)}{\omega - \xi + \hbar\omega_{\rm LO} + i\eta}\right].\end{aligned} \tag{17}$$

To obtain the last expression, we used a constant density-of-states approximation with $\rho(0)$ being the density of states at the Fermi energy per spin. We note that the above expression for the electronic self-energy, which goes beyond the zero-temperature limit at equilibrium, is essential for the discussion of mass enhancement at high temperatures. In the high-temperature limit, the energy being close to the Fermi energy, the Fermi-Dirac distribution function can be approximated as $n_{\rm FD}(\pm\xi,T_e) = 1/2$. This leads to the effective mass $m^*/m_b \approx 1 + \lambda$, where

$$\lambda = -\left.\frac{\partial\Sigma'(\omega)}{\partial\omega}\right|_{\omega\to 0} = g^2\rho(0)\left[n_B(\omega_{\rm LO},T_{\rm LO}) + \frac{1}{2}\right]I(\omega_{\rm LO}) \tag{18}$$

with

$$I(\omega_{\rm LO}) = \int d\xi\left[\frac{1}{(\xi + \hbar\omega_{\rm LO})^2} + \frac{1}{(\xi - \hbar\omega_{\rm LO})^2}\right]. \tag{19}$$

For the perovskite considered in the present work, the effective hot phonon frequency is about 3.45 THz (14.3 meV) [10]. For the fluence of 18 μJ/cm^2, if the hot phonon temperature increases from the base (room) temperature to reach equilibration with the electron temperature (about 550 K) at 1 ps, the enhancement $\delta\lambda/\lambda(T_L)$ becomes 81%. This is consistent with the approximate 120% increase that we obtained from our earlier analysis, giving further credence to our conclusion. Our methodology thus enables us to disentangle the contributions of band mass and the electron-phonon coupling constant to the carrier (or polaronic) effective mass, and shows that the electron-phonon coupling constant increases by about 100% under the action of light. We note that the notion of using the momentum-independent effective mass m^* or band mass m_b is only meaningful when the energy dispersion around the band minimum varies quadratically with momentum.

Further evidence for the polaron effect is the Coulomb screening of photoexcited carriers, which will renormalize the Coulomb potential $V_{\rm bare}$ via the dielectric function $\tilde{\epsilon}$ by $V_{\rm eff}(\omega,\tau) = V_{\rm bare}/\tilde{\epsilon}(\omega,\tau)$ [10]. Figure 7 shows the free-carrier screening factor Re $[1/\tilde{\epsilon}]$ at 0.5 THz as a function of pump-probe delay, obtained from our frequency-resolved TRTS data (see Appendix B 1). The screening is stronger at short time delays and does not even recover toward its preexcitation value until about 1.3 ns, which agrees well with the evolution of m^* in Fig. 5, suggesting the existence of a strong and long-lasting polaronic effect.

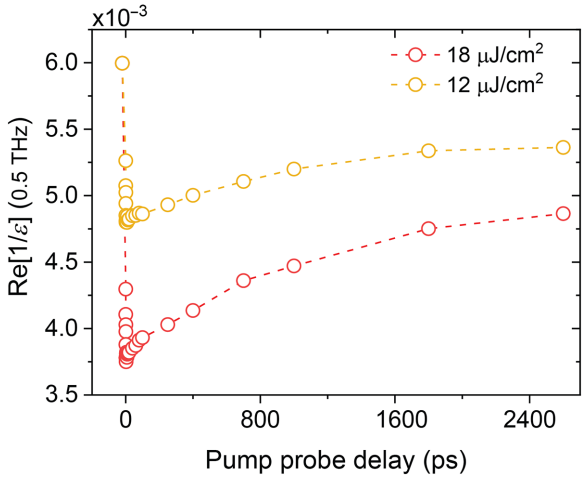

FIG. 7. Coulomb screening factor Re$[1/\tilde{\epsilon}]$ at 0.5 THz as a function of pump-probe delay.

III. CONCLUSION

We investigate the carrier dynamics in FCPIB perovskites by combining transient absorption spectroscopy and time-resolved terahertz spectroscopy. By fitting both the steady-state and transient absorption spectra to Elliott's model, we disentangle the carrier and exciton dynamics, and extract the physical parameters E_f (Fermi energy), E_g (band gap), and T_e (carrier temperature). At the same time, we perform the frequency-resolved and time-resolved terahertz spectroscopy, and, together with the TA results, obtain the time evolution of the effective mass m^*, and we observe a large and long-lived photoenhancement of m^*, which can be associated with the formation and decay of polarons. In addition, a microscopic model analysis reveals a twofold increase in the carrier-phonon coupling constant upon photoexcitation. Recently, the concept of liquid-crystal duality has been proposed to be the origin of the excellent photovoltaic properties of the halide perovskites [8]. Because of the cage nature of the crystal structure, plus the presence of soft phonons and organic cations, large polarons form easily. These large polarons enhance carrier screening, resulting in reduced Coulomb scattering from impurities, and, consequently, high defect tolerance, leading to a long diffusion length and carrier mobility [8–11,19]—both of which are crucial parameters for photovoltaic devices. All the aforementioned desirable photovoltaic properties therefore hinge on the formation of large polarons upon photoillumination. However, evidence of large polarons has been indirect, and no evidence has come from the most direct way of observing polarons—the carrier effective mass. Our work has not only estimated both the value and timescale of m^* after photoexcitation, but also obtained the photoinduced carrier-phonon coupling constant. We have seen that large m^* persists for a long time and that it reaches a maximum value around 200 ps after photoexcitation. In relation to energy research and technology, our work provides a methodology of verifying and quantifying polaronic effects, which can be applicable to broader photovoltaic materials than halide perovskites. For example, knowing that polaronic effects are strongest 200 ps after photoillumination, one can fabricate perovskite-based photovoltaic devices to time the carrier extraction process at 200 ps, harnessing the energy of hot carriers more efficiently.

ACKNOWLEDGMENTS

E.E.M.C acknowledges support from a Singapore Ministry of Education (MOE) AcRF Tier 2 grant (Grant No. MOE2019-T2-1-097). H.S. acknowledges financial support from Project AME-IRG-A20E5c0083. Y.M.L. acknowledges financial support from the Ministry of Education (MOE-T2-1-085). Work at Los Alamos was carried out under the auspices of the U.S. Department of Energy (DOE) National Nuclear Security Administration under Contract No. 89233218CNA000001, and was supported by the LANL LDRD Program. This work is supported in part by the Center for Integrated Nanotechnologies, a U.S. DOE BES user facility.

APPENDIX A: SAMPLE PREPARATION

A $FA_{0.85}Cs_{0.15}Pb(I_{0.97}Br_{0.03})_3$ thin film was grown by Dr. Chen Bingbing from Professor Lam Yeng Ming's group (MSE, NTU). The perovskite precursor solution is prepared by dissolving the precursors FAI, CsI, PbI_2, and $PbBr_2$ with respective stoichiometric ratio in a mixed organic solvent system comprising anhydrous N, N-dimethylformamide (DMF) and anhydrous dimethyl sulfoxide (DMSO) at the volume ratio of DMF:DMSO = 4:1. The z-cut substrate is cleaned with Hellmanex II solution(1% v/v), deionized water, acetone, and isopropyl alcohol in an ultrasonic bath for 15 mins, and then treated with an air plasma treatment for 15 mins and subsequently transferred to a nitrogen glove box for the deposition of perovskite films. The perovskite film is prepared by spin coating the perovskite solution (0.5 mol/L) on a quartz substrate at 1000 rpm for the first 10 s and 4000 rpm for the following 30 s. Chlorobenzene (200 μL) is dripped fast on the sample surface at 15 s before finishing the spin coating. The substrate is immediately placed on a hotplate for thermal annealing at 80 °C for 5 mins, then 120 °C for 5 mins, and then 180 °C for 30 mins.

APPENDIX B: EXPERIMENTAL METHODS

1. Frequency-resolved and time-resolved terahertz spectroscopy

Time-resolved terahertz spectroscopy is performed using a home-built setup. The terahertz probe beam with frequency range 0.5–2.5 THz is generated in a 1-mm-thick ZnTe crystal through optical rectification, transmitted

through the perovskite thin film, and then detected by electro-optical sampling in another ZnTe crystal with a 800-nm gating pulse. The pump-probe delay between the 400-nm pump pulse and the terahertz pulse, and the gate time delay between the terahertz pulse and the 800-nm-gating pulse are controlled by varying two motorized delay stages. By modulating both the 400-nm pump and terahertz probe beams, the transmitted terahertz electric field E and its photoinduced change ΔE are simultaneously measured with two lock-in amplifiers.

For the analysis of terahertz time-domain data, we calculate the complex electric field in the frequency domain for the sample $\tilde{E}_s(\omega)$ and the reference $\tilde{E}_r(\omega)$ to get the complex transmission coefficient $\tilde{T}(\omega) = \tilde{E}_s(\omega)/\tilde{E}_r(\omega)$. The complex refractive index $\tilde{n} = n + i\kappa$ can be extracted from $\tilde{T}(\omega)$ by solving the equation

$$\tilde{T}(\omega) = \frac{2\tilde{n}(\tilde{n}_{\text{sub}} + 1)\exp[i\omega d(\tilde{n} - 1)/c]\exp[-i\omega\Delta L(\tilde{n}_{\text{sub}} - 1)/c]}{(1 + \tilde{n})(\tilde{n} + \tilde{n}_{\text{sub}}) + (\tilde{n} - 1)(\tilde{n}_{\text{sub}} - \tilde{n})\exp[2i\omega d\tilde{n}/c]}, \tag{B1}$$

where $\tilde{n}_{\text{sub}}$ is the complex refractive index of z-cut quartz, c is the speed of light in vacuum, d is the film thickness, and ΔL is the thickness difference between the sample and reference substrates. It is noted that this equation is the exact formula applied to any thin film on a substrate, without having to consider the thin-film approximation [44].

From the frequency-resolved data, we can extract the complex refractive index of the FCPIB film and thus obtain the refractive dielectric function $\tilde{\epsilon}$ by $\tilde{\epsilon} = \tilde{n}^2$, where $\tilde{n} = n + i\kappa$ is the complex refractive index. From this, we can obtain $\text{Re}[1/\tilde{\epsilon}]$, as shown in Fig. 7.

2. Steady-state absorption spectra measurement

The steady-state absorption spectra measurement is performed using variable angle spectroscopic ellipsometry in the transmission mode. The film sample is illuminated by a halogen lamp and the transmitted light is then resolved by a monochromater and collected by silicon and InGaAs detectors.

3. Transient absorption measurement

Transient absorption spectra are measured using the commercial Helios Fire system from Ultrafast Systems. The 400-nm pump beam is produced from an 800-nm femtosecond laser (35-fs pulse width, 1-kHz repetition rate, 4-mJ pulse energy) passing through a beta barium borate crystal. The white-light probe is produced by focusing the 800-nm laser pulses on a sapphire crystal.

APPENDIX C: ENERGY RELAXATION FITTING

The electron-phonon scattering time is obtained by [45]

$$\tau_{\text{ave}} = \left[\frac{e^2\omega_{\text{LO}}}{2\pi\hbar}\left(\frac{m^*}{2\hbar\omega_{\text{LO}}}\right)^{1/2}\left(\frac{1}{\epsilon_\infty} - \frac{1}{\epsilon_s}\right)\right]^{-1}. \tag{C1}$$

The carrier-phonon coupling constant α is calculated via [10]

$$\alpha = \sqrt{\frac{m^* e^4}{2\hbar^2\epsilon_*^2\hbar\omega_{\text{LO}}}}, \tag{C2}$$

where $1/\epsilon_* = 1/\epsilon_\infty - 1/\epsilon_s$ and m^* is the carrier effective mass. With Eqs. (C1) and (C2), we can obtain

$$\alpha = \tau_{\text{ave}}^{-1} \Big/ \left(\frac{\omega_{\text{LO}}}{2\pi}\right). \tag{C3}$$

From Eq. (C3), we can then evaluate the carrier-phonon coupling strength α from the electron-phonon scattering time τ_{ave}.

[1] J. M. Ziman, *Electrons and Phonons: the Theory of Transport Phenomena in Solids* (Oxford University Press, Oxford, New York, 2001).

[2] G. Dresselhaus, A. F. Kip, and C. Kittel, Cyclotron resonance of electrons and holes in silicon and germanium crystals, Phys. Rev. **98**, 368 (1955).

[3] A. Damascelli, Z. Hussain, and Z.-X. Shen, Angle-resolved photoemission studies of the cuprate superconductors, Rev. Mod. Phys. **75**, 473 (2003).

[4] M. Schubert, P. Kühne, V. Darakchieva, and T. Hofmann, Optical Hall effect—model description: Tutorial, J. Opt. Soc. Am. A **33**, 1553 (2016).

[5] C. Q. Xia, M. Monti, J. L. Boland, L. M. Herz, J. Lloyd-Hughes, M. R. Filip, and M. B. Johnston, Hot electron cooling in InSb probed by ultrafast time-resolved terahertz cyclotron resonance, Phys. Rev. B **103**, 245205 (2021).

[6] Y. Yang, D. P. Ostrowski, R. M. France, K. Zhu, J. Van De Lagemaat, J. M. Luther, and M. C. Beard, Observation of a hot-phonon bottleneck in lead-iodide perovskites, Nat. Photon. **10**, 53 (2016).

[7] D. Zhao and E. E. M. Chia, Free carrier, exciton, and phonon dynamics in lead-halide perovskites studied

with ultrafast terahertz spectroscopy, Adv. Opt. Mater. **8**, 1900783 (2020).

[8] K. Miyata, T. L. Atallah, and X. Zhu, Lead halide perovskites: Crystal-liquid duality, phonon glass electron crystals, and large polaron formation, Sci. Adv. **3**, e1701469 (2017).

[9] E. Cinquanta, D. Meggiolaro, S. G. Motti, M. Gandini, M. J. P. Alcocer, Q. A. Akkerman, C. Vozzi, L. Manna, F. De Angelis, A. Petrozza, and S. Stagira, Ultrafast THz Probe of Photoinduced Polarons in Lead-Halide Perovskites, Phys. Rev. Lett. **122**, 166601 (2019).

[10] D. Zhao, H. Hu, R. Haselsberger, R. A. Marcus, M. Michel-Beyerle, Y. M. Lam, J.-X. Zhu, C. La-o-vorakiat, M. C. Beard, and E. E. M. Chia, Monitoring electron–phonon interactions in lead halide perovskites using time-resolved THz spectroscopy, ACS Nano **13**, 8826 (2019).

[11] T. Ivanovska, C. Dionigi, E. Mosconi, F. De Angelis, F. Liscio, V. Morandi, and G. Ruani, Long-lived photoinduced polarons in organohalide perovskites, J. Phys. Chem. Lett. **8**, 3081 (2017).

[12] B. Guzelturk, T. Winkler, T. W. Van de Goor, M. D. Smith, S. A. Bourelle, S. Feldmann, M. Trigo, S. W. Teitelbaum, H. G. Steinrück, G. A. D. L. Pena, R. Alonso-Mori, D. L. Zhu, T. Sato, H. I. Karunadasa, M. F. Toney, F. Deschler, and A. M. Lindenberg, Visualization of dynamic polaronic strain fields in hybrid lead halide perovskites, Nat. Mater. **20**, 618 (2021).

[13] E. Menéndez-Proupin, P. Palacios, P. Wahnón, and J. C. Conesa, Self-consistent relativistic band structure of the $CH_3NH_3PbI_3$ perovskite, Phys. Rev. B **90**, 045207 (2014).

[14] M. R. Filip, C. Verdi, and F. Giustino, Gw band structures and carrier effective masses of $CH_3NH_3PbI_3$ and hypothetical perovskites of the type $APbI_3$: A = NH_4, PH_4, AsH_4, and SbH_4, J. Phys. Chem. C. **119**, 25209 (2015).

[15] G. Giorgi, J. Fujisawa, H. Segawa, and K. Yamashita, Small photocarrier effective masses featuring ambipolar transport in methylammonium lead iodide perovskite: A density functional analysis, J. Phys. Chem. Lett. **4**, 4213 (2013).

[16] A. Amat, E. Mosconi, E. Ronca, C. Quarti, P. Umari, M. K. Nazeeruddin, M. Grätzel, and F. De Angelis, Cation-induced band-gap tuning in organohalide perovskites: Interplay of spin–orbit coupling and octahedra tilting, Nano Lett. **14**, 3608 (2014).

[17] P.-P. Sun, Q.-S. Li, L.-N. Yang, and Z.-S. Li, Theoretical insights into a potential lead-free hybrid perovskite: Substituting Pb^{2+} with Ge^{2+}, Nanoscale **8**, 1503 (2016).

[18] J.-P. Yang, M. Meissner, T. Yamaguchi, X.-Y. Zhang, T. Ueba, L.-W. Cheng, S. Ideta, K. Tanaka, X.-H. Zeng, N. Ueno, and S. Kera, Band dispersion and hole effective mass of methylammonium lead iodide perovskite, Solar RRL **2**, 1800132 (2018).

[19] K. Miyata, D. Meggiolaro, M. T. Trinh, P. P. Joshi, E. Mosconi, S. C. Jones, F. De Angelis, and X. Zhu, Large polarons in lead halide perovskites, Sci. Adv. **3**, e1701217 (2017).

[20] S. A. Bretschneider, I. Ivanov, H. I. Wang, K. Miyata, X. Zhu, and M. Bonn, Quantifying polaron formation and charge carrier cooling in lead-iodide perovskites, Adv. Mater. **30**, 1707312 (2018).

[21] M. Park, A. J. Neukirch, S. E. Reyes-Lillo, M. Lai, S. R. Ellis, D. Dietze, J. B. Neaton, P. Yang, S. Tretiak, and R. A. Mathies, Excited-state vibrational dynamics toward the polaron in methylammonium lead iodide perovskite, Nat. Commun. **9**, 1 (2018).

[22] See supplemental material at http://link.aps.org/supplemental/10.1103/PRXEnergy.2.013001 for details on experiments, data analysis, and Refs. [12,23].

[23] T. L. Cocker, D. Baillie, M. Buruma, R. J. Elliott, L. V. Titova, R. D. Sydora, F. Marsiglio, F. A. Hegmann, Microscopic origin of the Drude-Smith model, Phys. Rev. B **96**, 205439 (2017).2469-9950

[24] R. J. Elliott, Intensity of optical absorption by excitons, Phys. Rev. **108**, 1384 (1957).

[25] M. S. Dresselhaus, *Solid state physics. Part II. Optical properties of solids* (Massachusetts Institute of Technology, Cambridge, MA, 2001).

[26] M. Saba, M. Cadelano, D. Marongiu, F. Chen, V. Sarritzu, N. Sestu, C. Figus, M. Aresti, R. Piras, and A. G. Lehmann, *et al.*, Correlated electron–hole plasma in organometal perovskites, Nat. Commun. **5**, 1 (2014).

[27] N. Sestu, M. Cadelano, V. Sarritzu, F. Chen, D. Marongiu, R. Piras, M. Mainas, F. Quochi, M. Saba, and A. Mura, *et al.*, Absorption F-sum rule for the exciton binding energy in methylammonium lead halide perovskites, J. Phys. Chem. Lett. **6**, 4566 (2015).

[28] Q. Chang, D. Bao, B. B. Chen, H. W. Hu, X. Chen, H. Sun, Y. M. Lam, J.-X. Zhu, D. M. Zhao, and E. E. M. Chia, Tracking carrier and exciton dynamics in mixed-cation lead mixed-halide perovskite thin films, Commun. Phys. **5**, 1 (2022).

[29] D. Huang, J.-I. Chyi, and H. Morkoc, Carrier effects on the excitonic absorption in GaAs quantum-well structures: Phase-space filling, Phys. Rev. B **42**, 5147 (1990).

[30] V. D'innocenzo, G. Grancini, M. J. P. Alcocer, A. R. S. Kandada, S. D. Stranks, M. M. Lee, G. Lanzani, H. J. Snaith, and A. Petrozza, Excitons versus free charges in organo-lead tri-halide perovskites, Nat. Commun. **5**, 1 (2014).

[31] W. Rehman, D. P. McMeekin, J. B. Patel, R. L. Milot, M. B. Johnston, H. J. Snaith, and L. M. Herz, Photovoltaic mixed-cation lead mixed-halide perovskites: Links between crystallinity, photo-stability and electronic properties, Energy Environ. Sci. **10**, 361 (2017).

[32] T. C. Sum, S. Chen, G. Xing, X. Liu, and B. Wu, Energetics and dynamics in organic–inorganic halide perovskite photovoltaics and light emitters, Nanotechnology **26**, 342001 (2015).

[33] D. P. McMeekin, G. Sadoughi, W. Rehman, G. E. Eperon, M. Saliba, M. T. Hörantner, A. Haghighirad, N. Sakai, L. Korte, andB. Rech, *et al.*, A mixed-cation lead mixed-halide perovskite absorber for tandem solar cells, Science **351**, 151 (2016).

[34] J. Fu, Q. Xu, G. Han, B. Wu, C. H. A. Huan, M. L. Leek, and T. C. Sum, Hot carrier cooling mechanisms in halide perovskites, Nat. Commun. **8**, 1 (2017).

[35] I. Hamberg, C. G. Granqvist, K.-F. Berggren, B. E. Sernelius, and L. Engström, Band-gap widening in heavily Sn-doped in_2O_3, Phys. Rev. B **30**, 3240 (1984).

[36] E. Burstein, Anomalous optical absorption limit in InSb, Phys. Rev. **93**, 632 (1954).

[37] K.-F. Berggren and B. E. Sernelius, Band-gap narrowing in heavily doped many-valley semiconductors, Phys. Rev. B **24**, 1971 (1981).
[38] A. Walsh, J. L. F. Da Silva, and S.-H. Wei, Origins of band-gap renormalization in degenerately doped semiconductors, Phys. Rev. B **78**, 075211 (2008).
[39] B. J. Foley, D. L. Marlowe, K. Sun, W. A. Saidi, L. Scudiero, M. C. Gupta, and J. J. Choi, Temperature dependent energy levels of methylammonium lead iodide perovskite, Appl. Phys. Lett. **106**, 243904 (2015).
[40] A. Francisco-López, B. Charles, O. J. Weber, M. I. Alonso, M. Garriga, M. Campoy-Quiles, M. T. Weller, and A. R. Goñi, Equal footing of thermal expansion and electron–phonon interaction in the temperature dependence of lead halide perovskite band gaps, J. Phys. Chem. Lett. **10**, 2971 (2019).
[41] J. W. Li, L. W. Yang, Z. F. Zhou, P. K. Chu, X. H. Wang, J. Zhou, L. T. Li, and C. Q. Sun, Bandgap modulation in ZnO by size, pressure, and temperature, J. Phys. Chem. C **114**, 13370 (2010).
[42] A. Miyata, A. Mitioglu, P. Plochocka, O. Portugall, J. T.-W. Wang, S. D. Stranks, H. J. Snaith, and R. J. Nicholas, Direct measurement of the exciton binding energy and effective masses for charge carriers in organic–inorganic tri-halide perovskites, Nat. Phys. **11**, 582 (2015).
[43] G. D. Mahan, *Many-Particle Physics* (Kluwer Academic/Plenum, Springer New York, NY, 2000), 3rd ed.
[44] C. La-o vorakiat, L. Cheng, T. Salim, R. A. Marcus, M.-E. Michel-Beyerle, Y. M. Lam, and E. E. M. Chia, Phonon features in terahertz photoconductivity spectra due to data analysis artifact: A case study on organometallic halide perovskites, Appl. Phys. Lett. **110**, 123901 (2017).
[45] D. Zanato, N. Balkan, B. K. Ridley, G. Hill, and W. J. Schaff, Hot electron cooling rates via the emission of LO-phonons in InN, Semicond. Sci. Technol. **19**, 1024 (2004).

Correction: The previously published order of authors was presented incorrectly and has been fixed.